Available online at www.sciencedirect.com
ScienceDirect
Earth and Planetary Science Letters 264 (2007) 151 – 166
EPSL
www.elsevier.com/locate/epsl

Mechanical controls on the deformation of continents at convergent margins

Pascal Audet*, A. Mark Jellinek, Hideharu Uno

Department of Earth and Ocean Sciences, University of British Columbia, 6339, Stores Road, Vancouver, BC, Canada V6T 1Z4

Received 30 March 2007; received in revised form 5 September 2007; accepted 17 September 2007
Available online 29 September 2007
Editor: C.P. Jaupart

Abstract

Spatial variations in the rigidity of continental plates (expressed in terms of an effective elastic thickness, T_e) can have a profound influence on the style of deformation of ocean–continent convergent margins. Depending on the spatial distribution of T_e, strains related to plate boundary forces can become concentrated where T_e is small. We calculate T_e and T_e anisotropy in western Canada by using and comparing the wavelet and multitaper coherence methods. In addition to a nearly stepwise change in T_e from the Cordillera to the craton, we show that weak axes of T_e anisotropy are parallel with most compressive directions of horizontal stress components and fast axes of upper mantle seismic anisotropy. Maxima in the magnitude of T_e anisotropy are spatially correlated with the locations of most earthquakes and the locations and directions of maxima in electrical anisotropy and conductivity. The pattern of brittle failure and seismicity is explained as a response to plate boundary forces acting on a plate of variable rigidity and is expected to induce the observed mechanical anisotropy and enhance the flow of crustal fluids, resulting in locally high electrical conductivities. Our combined results thus suggest for the first time that the elastic properties of continental lithosphere have a leading order influence on the deformation and evolution of convergent plate boundaries.

Keywords: elastic thickness; anisotropy; lithosphere; convergent margin; deformation

1. Introduction

At a continental convergent boundary long-term tectonic loading may deform a lithospheric plate permanently by two mechanisms: brittle failure in the cool upper part of the lithosphere and by effectively viscous flow in the hotter deeper regions. The maximum stress that can be supported by the lithosphere is thought to occur at the intersection of these regimes, the so-called brittle–ductile transition (Kohlstedt et al., 1995). Under a present-day stress regime brittle failure is apparent from seismicity. A number of studies have shown that the depth to which seismicity occurs (the seismogenic zone) plausibly corresponds to a lower bound to the elastic thickness, T_e, which for a lithostatic state of stress is the vertical fraction of the lithosphere that behaves elastically over geological time scales (Maggi et al., 2000; Watts and Burov, 2003). The flexural rigidity $D \propto ET_e^3$, where E is Young's modulus, is a rheological property that governs the resistance of the lithosphere to flexure by plate boundary forces (Watts, 2001). The strong dependence of D on T_e implies that the magnitude and spatial variations of T_e can have a significant influence on the degree and

* Corresponding author.
E-mail address: paudet@eos.ubc.ca (P. Audet).

0012-821X/$ - see front matter © 2007 Elsevier B.V. All rights reserved.
doi:10.1016/j.epsl.2007.09.024

style of deformation due to long-term tectonic loads. In particular, it is expected that spatial variations in T_e can prescribe where stress concentration may occur and consequently determine the location of earthquakes, as well as mechanical anisotropy, due to the localized brittle failure of crustal rocks (Lowry and Smith, 1995).

The mechanics governing the tectonic evolution of convergent plate boundaries remain a major focus of both observational (Peacock, 1990; Stern, 2002) and modelling (Becker et al., 1999; Billen et al., 2003; Stegman et al., 2006) studies of subduction zones. However, although potentially important, the influences of T_e variations on the rheology, dynamics and evolution of convergent margins are poorly understood (Burov and Diament, 1995; Gaspar-Escribano et al., 2001). A central reason is the difficulty in constraining spatial variations in T_e. Only a few studies (e.g. Flück et al., 2003; Rajesh et al., 2003) have focused on estimating T_e in active convergent tectonic settings using window-based methods. More recently, Tassara et al. (2007) used the wavelet method to calculate T_e in South America. In this study we calculate T_e and T_e anisotropy in western Canada by using and comparing the multitaper and wavelet transform methods. Western Canada is an ideal target for T_e studies because it has a rich and diverse tectonic history spanning ~3 Ga, where rigidity variations may have played a major role in continental evolution. This region encompasses three main tectonic domains: the young and tectonically active Phanerozoic Cordillera to the west, the Paleo-Proterozoic Interior Plains covered by a thick layer of Phanerozoic sediments, and the stable Archean Craton to the east. The tectonic evolution of the plate margin has been dominated by convergence since the Mezosoic (Price, 1986). The plate boundary at the western edge of the continent is currently defined by the subduction of the Juan de Fuca plate to the south, and the strike–slip Queen Charlotte fault system to the north.

To gain a sound understanding of the mechanical controls on the deformation of the lithosphere at convergent margins, T_e results should be compared with a range of geophysical indicators of lithospheric deformation (Eaton and Jones, 2006). In western Canada several experiments conducted by LITHOPROBE and POLARIS provide a wealth of seismic, magnetotelluric, and heat flow data. In this paper we start by using and comparing the multitaper and wavelet methods for estimating T_e and T_e anisotropy. We then compare the results with a range of geophysical observables from the same region. The geophysical correlations allow us to formulate a conceptual model of deformation at convergent margins that can be tested in future studies of lithospheric dynamics.

2. T_e estimation

2.1. Coherence method

T_e is estimated by minimizing the misfit (L2 norm) between the observed spectral coherence between topography and Bouguer gravity anomalies and the coherence predicted for the flexure of a uniform elastic plate bending under the weights of topography at the surface and internal loads related to density variations (Watts, 2001). The plate response is modelled either as isotropic or anisotropic, and the coherence is inverted for a single parameter, T_e, or the three parameters of an assumed orthotropic elastic plate (i.e. having different rigidities in two perpendicular directions), T_{min}, T_{max}, and ϕ, the direction of weakest rigidity (Swain and Kirby, 2003). The coherence is an averaging property which measures the consistency of the phase dependence between two signals or fields at distinct wavelengths. Applied to topography and gravity data sets, it provides a measure of the degree of flexural compensation of tectonic loads. An important physical parameter for understanding this property is the characteristic flexural wavelength,

$$\lambda_F \sim \left(\frac{ET_e^3}{\Delta\rho g}\right)^{1/4} \tag{1}$$

where $\Delta\rho$ is the density contrast at the depth of compensation, g is the gravitational acceleration, and "~" means "scales as". At short wavelengths ($\lambda \ll \lambda_F$) the loads are fully supported by elastic stresses and the Bouguer anomaly is not coherent with the topography. In contrast, at long wavelengths ($\lambda \gg \lambda_F$) loads are compensated isostatically and the Bouguer anomaly is coherent with topography. Typical coherence curves vary smoothly from 0 to 1, reflecting the transition from flexurally-supported to fully compensated loads. In particular, Eq. (1) indicates that the wavelength of transition from compensated to uncompensated loads increases for increasing plate rigidity.

In the continents the elastic thickness estimated using the coherence method ranges between very low (T_e < 10 km) and very high (T_e > 100 km) values, reflecting the wide variety of tectonic settings and the thermal evolution of the lithosphere (Pérez-Gussinyé et al., 2004). Discrepancies occur, however, when the results from different spectral estimation and load deconvolution techniques applied to the same datasets are compared (Pérez-Gussinyé et al., 2004; Audet and Mareschal, 2007). This problem arises because T_e is a wavelength dependent parameter (Eq. (1)), and the accuracy of its estimation is controlled by the spatio-spectral resolution of the analysis technique. Window-based methods have good resolution in frequency, but lack spatial resolution, depending on window width. Spatio-spectral (or space-scale) methods, on the other hand, offer a compromise on the resolution in both reciprocal domains, and are thus able to characterize spatial discontinuities. It is thus important to use and compare different spectral methods whenever possible.

In contrast to most previous analyses of T_e, generally relying on a single spectral technique (e.g. Lowry and Smith, 1995; Simons et al., 2000; Kirby and Swain, 2006; Audet and Mareschal, 2007), we maximize both spatial and wavelength resolutions by using and comparing two spectral techniques for the calculation of the coherence and the estimation of T_e: the multitaper (Simons et al., 2000; Pérez-Gussinyé et al., 2004) and wavelet transform (Kirby and Swain, 2006; Audet and Mareschal, 2007) methods. Applied to western Canada, we show that both techniques recover the spatial pattern of T_e and the T_e anisotropy, but the wavelet method provides both better spatial resolution and higher absolute estimates of T_e.

In the inversion, the predicted coherence is calculated by deconvolving the topography and Bouguer anomaly into surface and internal components of the initial loading structure (Forsyth, 1985). See Pérez-Gussinyé et al. (2004) for the details of this calculation. This step requires information on the crustal structure (Moho depth and density contrasts) that we extract from the LITH5.0 crustal model (Perry et al., 2002). We take the subsurface load to be the density contrast at the Moho (Watts, 2001).

The flexural rigidity is converted to T_e using a Poisson ratio of 0.25 and Young modulus of 100 GPa. Resolution tests and statistical analysis of estimated T_e values from synthetic modelling show that the accuracy of recovered T_e strongly depends on the size of the window compared to the flexural wavelength (Audet and Mareschal, 2007), which is expected from Eq. (1). A reasonable estimate of the accuracy of T_e estimated from spectral methods is $\pm 15\%$ of the recovered value. Moreover, as T_e is sensitive to a range of parameters (Burov and Diament, 1995; Lowry and Smith, 1995), additional uncertainties in the choice of material parameters and modelling approaches can be described as log-normal and of the order 30%–50% (Lowry and Smith, 1995). Since only major trends are of interest, the variance of T_e estimates will not affect the interpretation of the results.

2.2. Multitaper analysis

The multitaper analysis is performed using a set of orthogonal basis functions that minimize the variational problem of broadband bias reduction as data tapers (Thomson, 1982), such that multiple estimates of the same spectrum are approximately uncorrelated and can be averaged to reduce the estimation variance. The set of functions is characterized by two numbers: the time-frequency bandwidth product NW that controls the wavelength resolution and spectral leakage, and the number of significant tapers k that governs the estimation variance. The multitaper spectral estimates are calculated using Discrete Prolate Spheroidal Slepian (DPSS) tapers with $NW=3$ and $k=3$ throughout this study. See Pérez-Gussinyé et al. (2004) for the description of the general application of the multitaper method in T_e studies.

In the multitaper method, the load deconvolution is done in a given rectangular window of the study area and the estimated T_e value is assigned to the area covered by the window (Pérez-Gussinyé et al., 2004). Spatial resolution is achieved by moving the windows over the entire data set with some overlap. The size d of the data windows is critical in the estimation of T_e because small windows provide high spatial resolution but cannot resolve long flexural wavelengths (c.f. Eq. (1), $d < \lambda_F$), while large windows (i.e. $d \gg \lambda_F$) provide an average of the true distribution of T_e within the window, thus degrading the spatial resolution. Although a popular method (Pérez-Gussinyé et al., 2004), two important limitations of the multitaper method for T_e estimation emerge because of the trade-off between window size and frequency resolution and cause: (1) limited spatial and wavelength resolution, and (2) lower estimates of T_e. To counter these effects, we map out results using a combination of window sizes of 300×300 km^2, 500×500 km^2, and 800×800 km^2 (shown at lower left corner of Fig. 3a), with an overlap of 70% between adjacent windows. When the misfit does not converge, we assign a value of 60 km to the window, which is the largest resolvable T_e value using the 800×800 km^2 window. Results are extrapolated to the edges of the study area and the maps are averaged. The spatial recovery of T_e is limited by the size of the smallest window and is restricted to a 1484×1484 km^2 square region in the center of the study area. Finally, the resulting map is filtered using a Gaussian function of width 140 km to produce a continuous image of T_e that is more easily comparable to the results obtained with the wavelet transform method. Results do not change for Gaussian functions with different window widths.

The multitaper method also allows for the determination of directional variations of the coherence because the spectra are effectively calculated and averaged at each wavevector (k_x, k_y) in the 2D spectral plane. The results of the inversion for the anisotropic T_e cannot be averaged spatially as in the isotropic analysis (above), because the weak directions can vary between estimates obtained with different window sizes. However the results can be qualitatively compared with those obtained with the wavelet method (below) to assess the general trends seen in the map of T_e anisotropy.

2.3. Wavelet transform

In the wavelet analysis there is no need for fixed spatial window because the wavelet transform, defined as the convolution of a signal with a scaled and rotated kernel called a wavelet, is a space-scale operation that calculates the spectra at each grid point. The convolution is performed over the entire grid of the study area at different scales, which are related to a Fourier wavenumber. In this study we use the directional 2D Morlet wavelet because it is well suited for the study of T_e and the anisotropy (Kirby and Swain, 2006; Audet and Mareschal, 2007). The Fourier load deconvolution of Forsyth (1985) is performed at each grid point by making

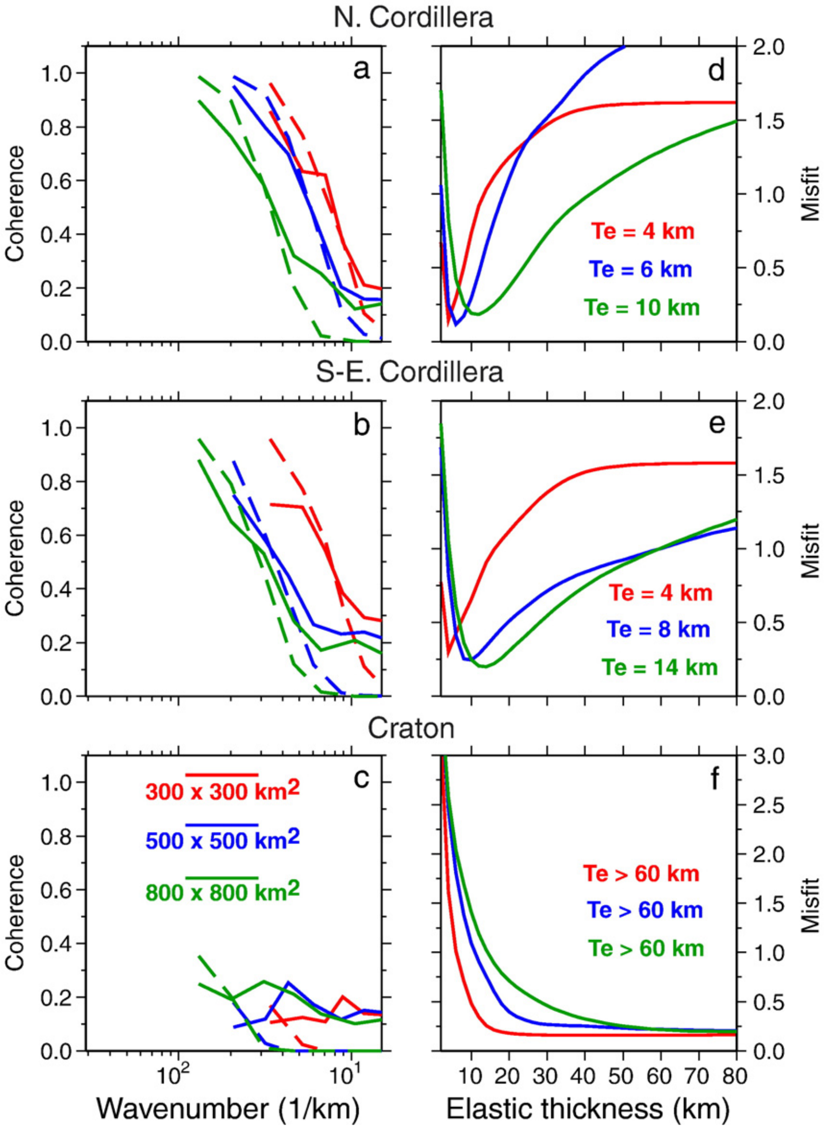

Fig. 1. Examples of T_e estimated with the multitaper method for the three window sizes: a–c) Observed (solid lines) and predicted (dashed lines) coherence curves for three locations in western Canada ((a) North Cordillera, (b) South-East Cordillera, and (c) Craton); d–f) L2 norm (root mean square) error between observed and predicted coherence curves for a range of T_e values and for each window used. Sizes of windows are 300×300 km^2 (red curves), 500×500 km^2 (blue curves), and 800×800 km^2 (green curves). (For interpretation of the references to colour in this figure legend, the reader is referred to the web version of this article.)

the assumption of spatial decoupling between adjacent local wavelet spectra (Stark et al., 2003; Kirby and Swain, 2004; Audet and Mareschal, 2007). In other words, we assume that the wavelet coefficients at one grid point are statistically independent from neighboring coefficients, and apply a Fourier-based deconvolution to the wavelet spectra. In reality, however, spatial and spectral (space-conjugate) resolutions trade-off in the wavelet analysis as implied by the uncertainty principle in information theory, which states that physical and spectral localizations cannot be measured simultaneously with arbitrarily high precision. Short-scale wavelets are well localized in space but broad in the spectral domain. Large-scale wavelets are well localized in the spectral domain but broad in space. This results in a smoothed version of T_e where it is large, but allows for larger estimates of T_e than the multitaper method due to the presence of longer wavelengths contributing to the spectra.

In the anisotropic analysis, the coherence is calculated at distinct azimuths using a directional Morlet wavelet (Kirby and Swain, 2006; Audet and Mareschal, 2007) on a coarse grid for a better visualization of the variations of the weak axes. See Audet and Mareschal (2007) or Kirby and Swain (2006) for the description of the application of the wavelet transform method in T_e studies.

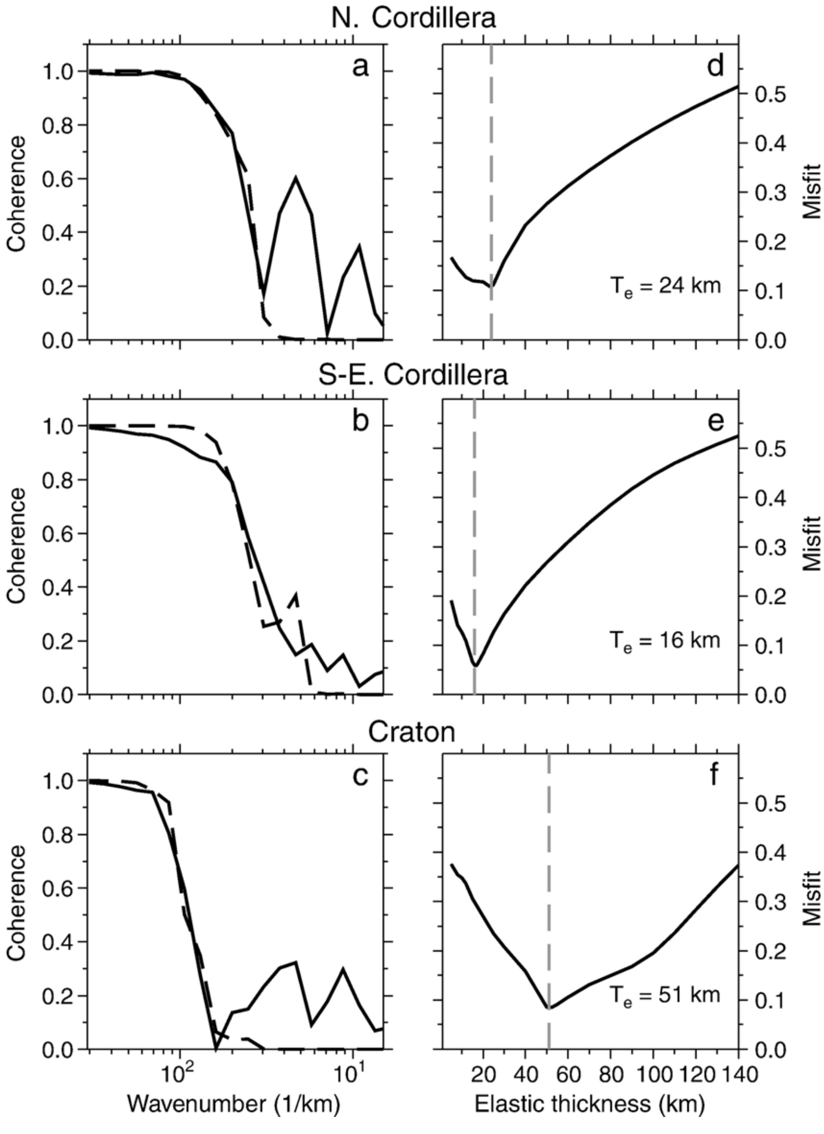

Fig. 2. Examples of T_e estimated with the wavelet transform method for the three locations indicated on the plots. The coherence curves show the characteristic roll-over from uncompensated (0 coherence) to fully compensated (coherence of 1) loads as well as a clear minimum misfit in all cases.

3. Results

3.1. Isotropic T_e

Fig. 1 shows example results of the 1D (azimuthally averaged) multitaper coherence for the three window sizes at different locations (N. Cordillera, S-E Cordillera, and Craton). Misfit curves show a clear minimum for small values of T_e even for the smallest window used. As the size of the window increases, more wavelength information from neighboring regions is retained in the coherence and the estimate can vary by as much as a factor of 5. In the Craton the maximum of the coherence curves remains small even for the largest window size, and the misfits do not converge to a stable T_e value, indicating that T_e is large in this region. In comparison, the wavelet coherence shows the characteristic roll-over from uncompensated (0 coherence) to fully compensated (coherence of 1) loads as well as a clear minimum misfit in all cases (Fig. 2).

Multitaper and wavelet maps of T_e are shown in Fig. 3. Regardless of the technical differences between the two methods, qualitatively, the results agree encouragingly well and correlate with major physiographic provinces in western Canada. T_e varies from <30 km in the Phanerozoic Cordillera to >60 km in the Paleo-Proterozoic Craton over a distance of a few hundred kilometers. This trend is in qualitative agreement with a previous study of T_e in western Canada that used the maximum entropy spectral estimator (Flück et al., 2003), although the maximum estimates of T_e in the Craton are generally a factor 2 to 3 smaller.

Despite a good overall qualitative agreement between the T_e maps, there is a pronounced difference in the Craton where multitaper estimates are lower than 30 km in some instances. The discrepancies stem in part from the ad hoc methodology adopted in Section 2.2 for the mapping of the windowed multitaper estimates, and from the difference in spatial and spectral resolutions between the two methods. In the Craton T_e is presumably large, such that small windows would not resolve the transition wavelength from low to high coherence. However, high coherence (>0.3, c.f. Fig. 1) at short wavelengths (the “spurious” coherence mentioned in Swain and Kirby (2006) and Audet and Mareschal (2007)) not associated

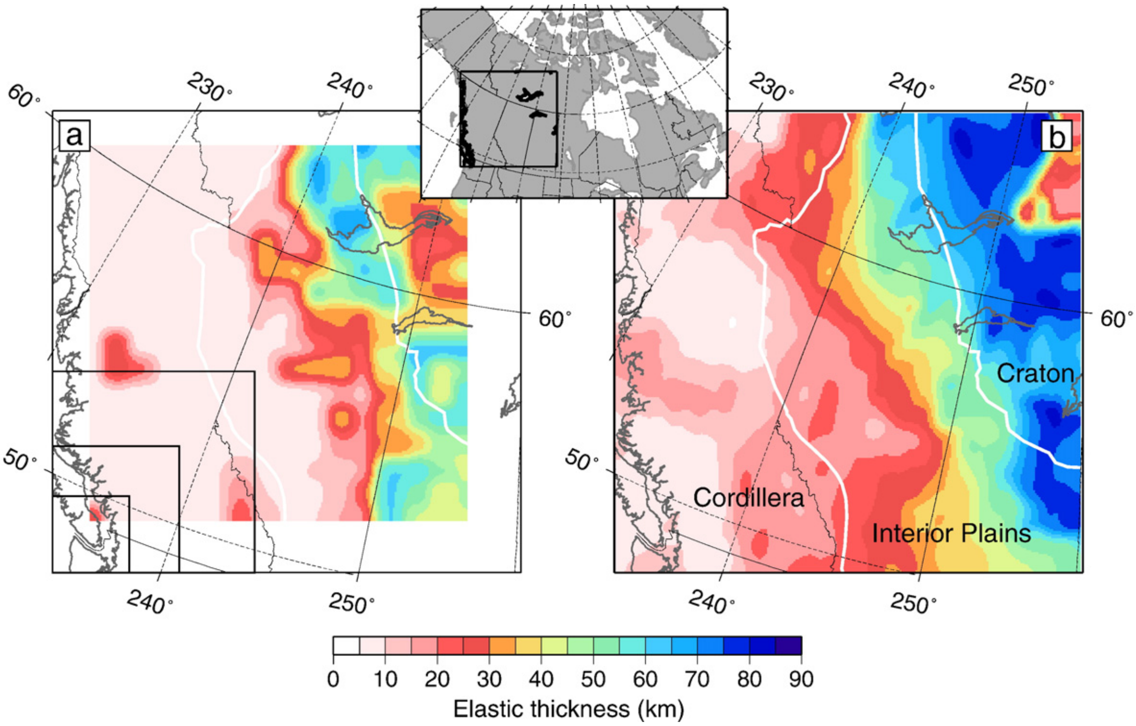

Fig. 3. T_e structure of western Canada calculated from the coherence between Bouguer gravity and topography using the multitaper (a) and the wavelet transform (b) methods. Data are projected onto a Transverse Mercator grid. Although the values differ in (a) and (b), the qualitative T_e structure is approximately equivalent, in particular the location of the T_e gradient. The T_e results from the multitaper method are lower than those obtained with the wavelet method due to the use of moving windows of different sizes (shown by the boxes at the lower left corner in (a)) which limits the spatial and wavelength resolutions (Simons et al., 2000). Thus, we consider the wavelet results to be more reliable. Major physiographic provinces are bounded by solid white lines. The results show a well-defined transition from low values in the Cordillera, intermediate values in the buried Interior Plains, and high values in the exposed Craton. Inset shows the location of the study area with respect to North America.

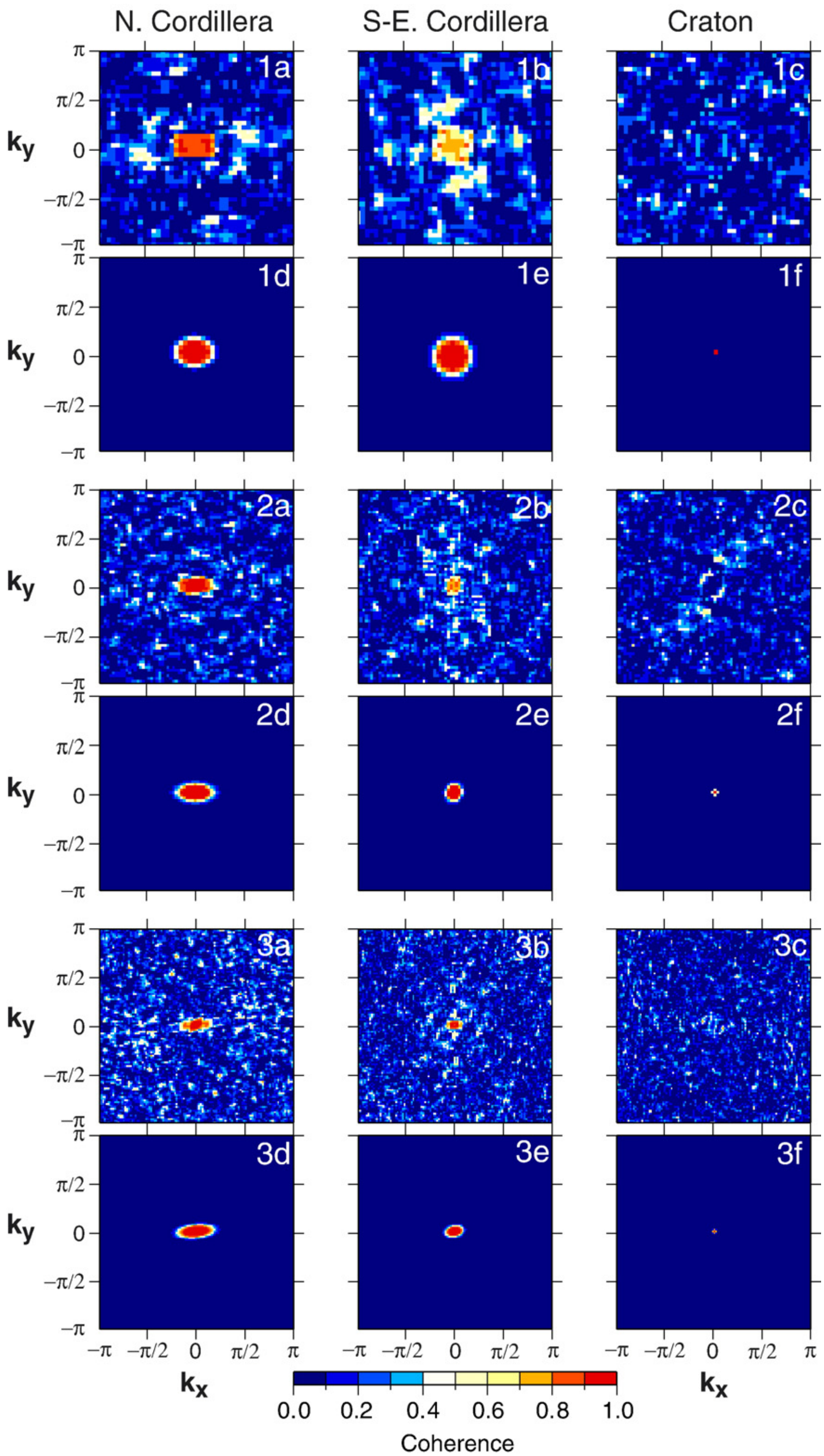

Fig. 4. Anisotropic inversion of T_e using the multitaper method. Observed (a–c) and theoretical (d–f) 2D coherences using different windows: (1a–f) is 300×300 km^2; (2a–f) is 500×500 km^2; and (3a–f) is 800×800 km^2. Wavenumbers are normalized by each window size. The observed 2D coherences correspond to the three locations described in Fig. 1: (1–3a) N. Cordillera, (1–3b) S-E Cordillera, and (1–3c) Craton. The major axis of the high-coherence ellipse points in the direction of lower T_e, or T_{min}.

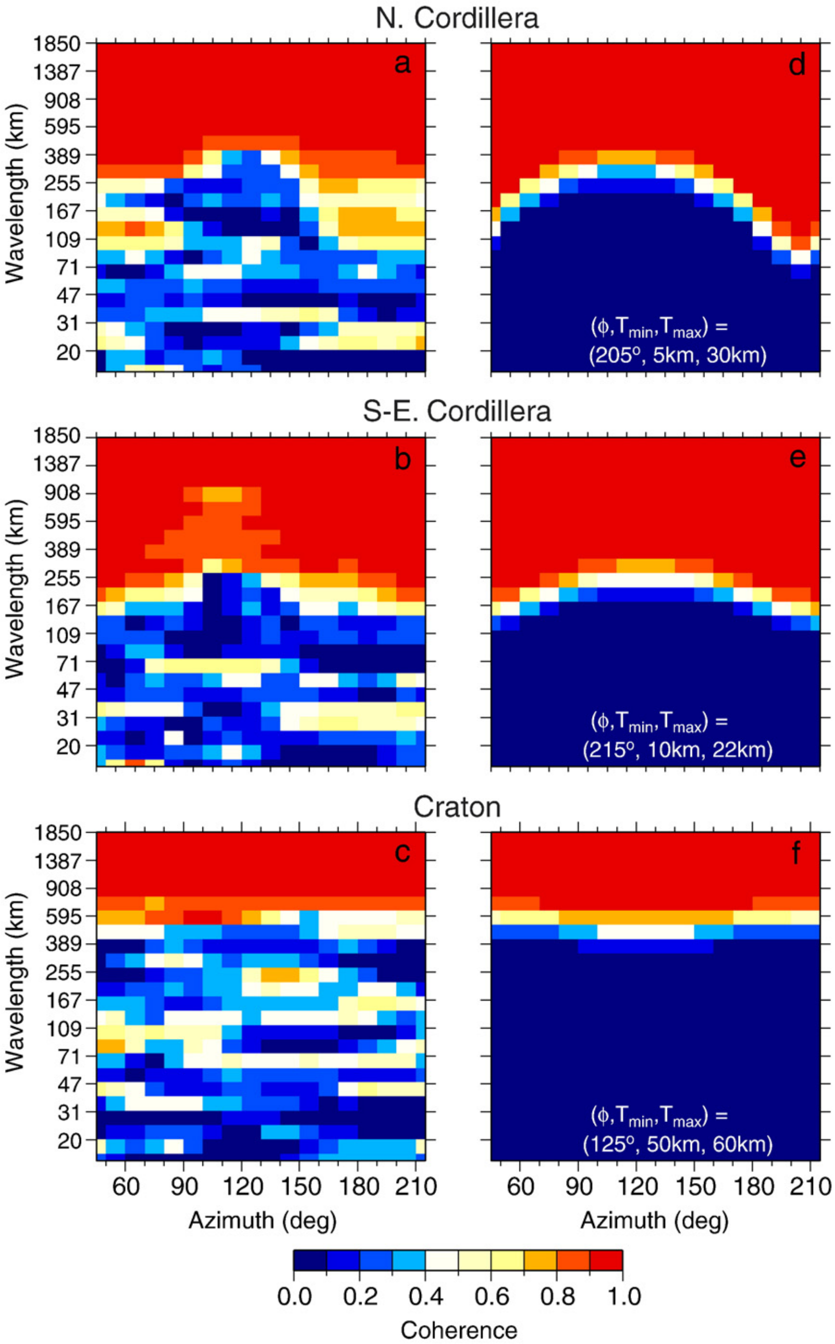

Fig. 5. Anisotropic inversion of T_e using the wavelet transform method. The coherence is plotted as function of wavelength and azimuth. Observed (a–c) and theoretical (d–f) 2D coherences for the three locations: (a) N. Cordillera, (b) S-E Cordillera, and (c) Craton. Legend in 2D theoretical plots indicates best-fitting parameters of the orthotropic elastic plate. The anisotropy is well developed in the N. Cordillera and in the S-E Cordillera, but almost absent in the Craton.

with the flexure of an elastic plate can be mapped as T_e and thus lower the T_e average over the region. The extent to which this short-wavelength anomaly affects the mapping of T_e is thus controlled by the spatial resolution: in the multitaper estimates, it will dominate the T_e mapping until a large enough window is able to resolve the flexural wavelength (c.f. Eq. (1), $d \sim \lambda_F$). This situation is amplified by the fact that our study area is small, and thus only a small number of the largest windows is used. In the wavelet method the deconvolution is performed at each grid point and thus incorporates less information from neighboring grid points. Because this high coherence is observed at short wavelengths, the mapping of the wavelet estimates of T_e is less affected by the spurious coherence.

Although a more careful picking of T_e estimates according to the T_e sensitivity for each window size (see for e.g. Flück et al., 2003; Pérez-Gussinyé et al., 2004) could perhaps erase this low-T_e anomaly, we prefer to avoid making any a priori assumption about the underlying T_e structure because this introduces an additional observational bias. Alternatively, Pérez-Gussinyé et al. (2007) calculated multitaper T_e estimates using three window sizes and produced three maps of T_e in South America that compared favorably with the wavelet method in the same region (Tassara et al., 2007). Another approach is to weight the misfit by the inverse of wavenumber, as was done in Kirby and Swain (2006), Swain and Kirby (2006) and Tassara et al. (2007). This filtering procedure downweights the contribution of the high coherence at small wavenumbers, effectively erasing the low-T_e anomaly, at the cost of spatial resolution (Kirby and Swain, 2006; Pérez-Gussinyé et al., 2007). We note that the wavelet map of T_e also shows an intriguing low-T_e region at the north-east corner of the study area, with a lesser spatial extent. Such low-T_e estimates due to short-wavelength coherence is also found elsewhere in the Canadian Shield (Audet and Mareschal, 2004, 2007). The origin of those features is beyond the scope of this study.

We suggest that a more thorough comparison between the wavelet and multitaper methods applied to T_e is needed in order to isolate the contribution of the methods themselves to the differences observed.

3.2. Anisotropic T_e

Fig. 4 shows example results for the anisotropic coherence calculated with the multitaper method at the same three locations as those in Fig. 1. Also shown are best-fitting 2D coherences using analytical solutions of the orthotropic elastic plate (Kirby and Swain, 2006; Audet and Mareschal, 2007). In a 2D wavenumber plot (k_x, k_y) of coherence, anisotropic T_e typically produces an elliptical shape of high coherence, whereas isotropic T_e appears as a circular region of high coherence. Fig. 4 indicates that the anisotropy is well-developed in the N. Cordillera as the results for the three window sizes are consistent. In the S-E Cordillera the coherence is quasi isotropic except for the estimate obtained with the largest window. The Craton estimates show an absence of coherence at the longest wavelengths as in the 1D case, indicating that still larger windows are necessary to resolve T_e and the anisotropy in this region.

The wavelet results (Fig. 5) are presented in 2D as wavelength–angle plots. The signature of anisotropic T_e is then characterized by a 180° periodic variation of high coherence, whereas the signature of isotropic T_e is a flat line. The wavelet results agree with the multitaper results and show that the anisotropy is well developed in the N. Cordillera and in the S-E Cordillera, but almost absent in

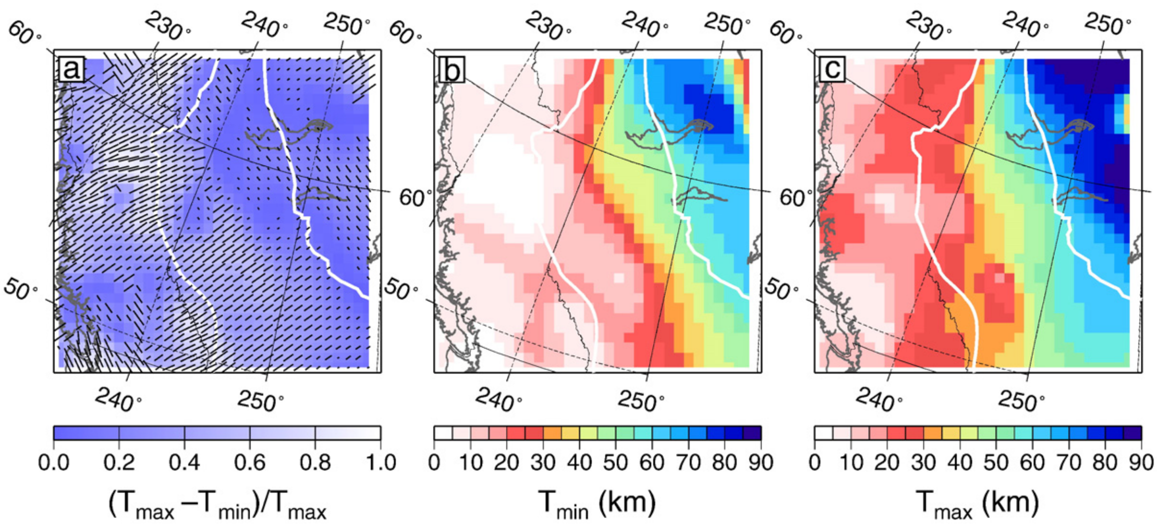

Fig. 6. Anisotropic T_e structure of western Canada from the wavelet transform method. The 2D coherence is inverted using the thin orthotropic plate model, i.e. having different rigidities in two perpendicular directions, for three parameters: the minimum (b) and maximum (c) values of T_e, and ϕ the orientation of the weak direction calculated anti-clockwise from the x-axis (a). The weak direction of mechanical anisotropy in (a) is plotted as thin solid black bars superposed on a color scale map of the anisotropic magnitude. The patterns of T_{min} and T_{max} closely mimic the isotropic T_e structure of Fig. 3. In particular, the maximum gradient occurs at the same location, and accompanies a change in both the magnitude and orientation of the weak direction.

the Craton. Maps of T_e anisotropy using the multitaper method show considerable scatter with the major trends described above, and we choose not to interpret them.

The resulting map of the anisotropic inversion of T_e using the wavelet method is shown in Fig. 6. The magnitude of T_e anisotropy is given by the ratio $(T_{max}-T_{min})/T_{max}$. T_e anisotropy is maximized in the Cordillera and across the Interior Plains where $T_e<30$ km, closely mimicking the isotropic T_e pattern. The mechanical weak (i.e. low rigidity) direction is dominantly SW–NE in this region, approximately perpendicular to the main belts of the Cordillera and parallel to the direction of Cascadia subduction. East of $T_e=30$ km contour, the T_e anisotropy progressively decreases in magnitude. In addition, the trend of the weak direction, ϕ, rotates to a SE–NW direction in the Craton and in the northernmost part of the Interior Plains. We note also that the maps of T_{min} and T_{max} follow closely the isotropic T_e structure of Fig. 3. In particular, the maximum gradient occurs at the same location.

3.3. Geophysical correlations

In Fig. 7a we plot the location of the highest T_e gradient using the wavelet results, along with the location of earthquake epicenters for all events with magnitude larger than M=3 that occurred since 1979. On the map is also shown a 150×1800 km^2 corridor trending SW–NE within which T_e, T_e gradient ($|\nabla T_e|$), and crustal thickness (T_c) were extracted and averaged, and plotted in Fig. 7b. Fig. 7c shows T_e with the percentage of seismicity and heat flow values along the same profile. The highest T_e gradient is found in the Interior Plains, 100 to 300 km west of the largest concentration of seismicity, and also where $T_e<30$ km. The position and magnitude of the T_e gradient also broadly correlate with a similar (i.e. factor of about 2) eastward decrease in vertical heat flux (Hyndman and Lewis, 1999), consistent with inferences from xenolith thermobarometry and seismic data (Currie and Hyndman, 2006). The T_e gradient corresponds also to a transition in crustal thickness from ~30 km in the Cordillera to >40 km in the Craton (Perry et al., 2002), and with a gradient of low to high S-wave seismic velocity anomalies imaged by seismic tomography (Frederiksen et al., 2001).

In Fig. 8a we plot the T_e weak directions along with seismic and magnetotelluric measurements of crustal and upper mantle anisotropy and indicators for crustal stresses. Fig. 8b shows the magnitude of the T_e anisotropy with averages of T_{min} and T_{max} along the same profile as Fig. 7. In the southern Cordillera and across the Interior Plains the fast axis of seismic anisotropy, as measured from SKS splitting data, show coherent fast polarizations in the SW–NE direction (Shragge et al., 2002; Currie et al., 2004). The geoelectric strikes align in the same direction as the SKS data (Boerner et al., 1999; Ledo and Jones, 2001). Both

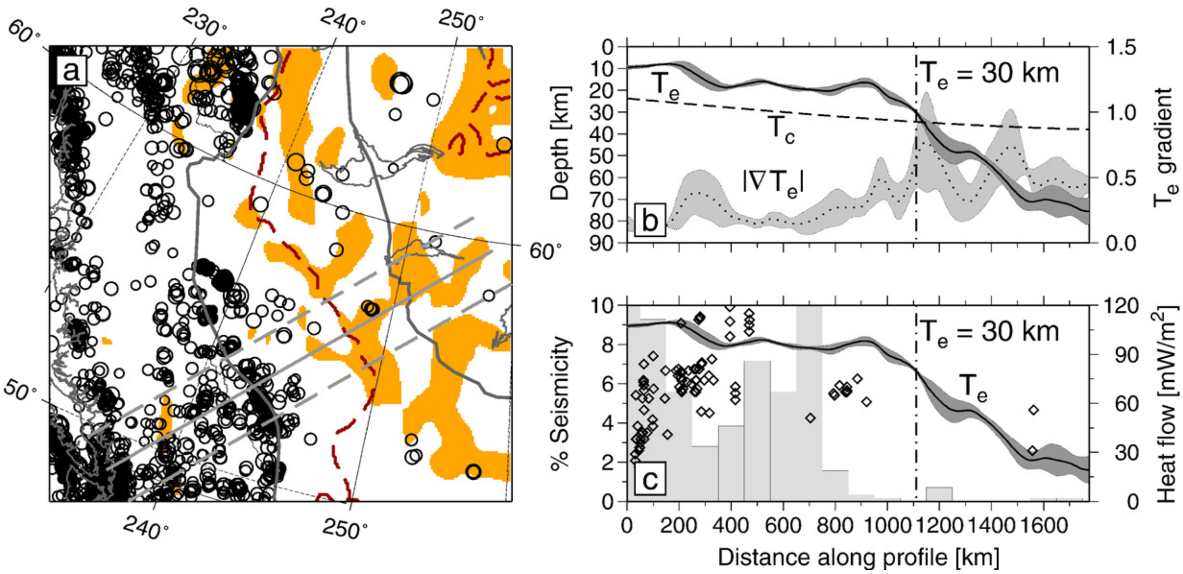

Fig. 7. Correlations between the T_e structure and geophysical data. In (a) the seismicity (with magnitude > 3) of western Canada, represented by black circles at earthquake epicenters recorded between 1979 and 2006, is plotted against the location of the maximum gradient of T_e shown in orange. Thick grey lines are the province boundaries. Dashed dark red line is the 30 km contour which roughly follows the maximum gradient limit. (b) shows the average of T_e, T_e gradient, and T_c calculated within the corridor delimited by the thick gray dashed lines in (a), and projected along the profile shown by the thick gray line. In (c) the T_e is plotted against the seismicity (gray bins) and heat flow values (diamonds) extracted within the same corridor and projected along the profile. The west–east decrease in seismicity correlates with the location of the T_e gradient, where $T_e\sim T_c\sim30$ km, and where heat flow decreases by a factor of 2.

anisotropy indicators align with the T_e weak directions and with the maximum horizontal compressive stress directions. This striking uniform pattern of anisotropy persists over a wide area to about 57° latitude, and correlates with a change in T_e from $T_e < T_c$ to $T_e > T_c$. This also corresponds to the boundary defined by the largest T_e gradient, where $T_e \sim 30$ km, and where the T_e anisotropy changes in both amplitude and direction.

In order to quantitatively compare the anisotropy datasets, we resampled the seismic, magnetotelluric and stress data onto the coarse T_e anisotropy grid. Fig. 9 shows histograms of the difference in angle between the T_e weak directions and the seismic, magnetotelluric, and stress directions, along with a histogram of percent alignment to within 15° and 22.5° (Simons and van der Hilst, 2003). Stress and magnetotelluric data show well-defined Gaussian curves centered on ~10° to 20° difference with T_e anisotropy (Fig. 9b,c), and the alignments are well above the 15° and 22.5° significance levels (Fig. 9d). The angle differences between T_e weak axes and seismic fast axes

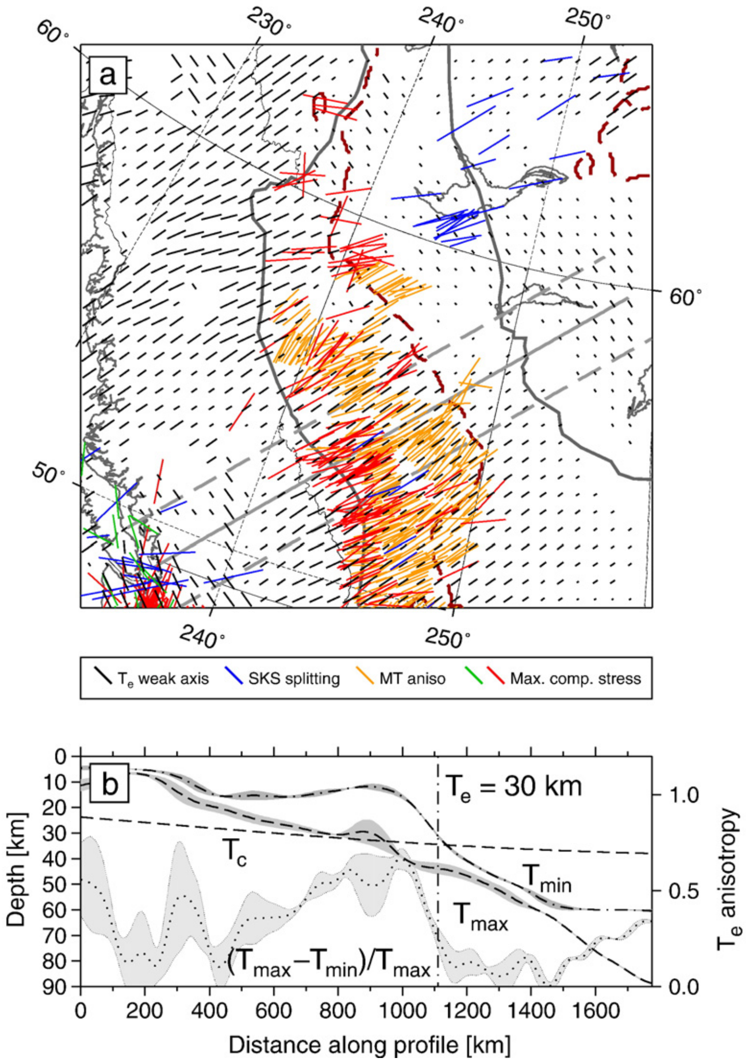

Fig. 8. Anisotropy correlations in western Canada. In (a) the mechanical weak axes (black bars) are plotted along with seismic (SKS splitting — blue bars (Shragge et al., 2002; Eaton et al., 2004; Currie et al., 2004), and electrical (geoelectric strikes — orange bars (Boerner et al., 1999)) anisotropy data. Green and red bars are maximum compressive horizontal stress directions inferred from shear-wave splitting above local earthquakes in the Cascadia forearc (Currie et al., 2001) and borehole breakouts, respectively. Dashed dark red line is the T_e=30 km contour. (b) shows the average of T_{min}, T_{max}, and the magnitude of T_e anisotropy calculated within the corridor and projected along the profile as in Fig. 7b,c. The boundary defined by $T_e \sim 30$ km correlates with a decrease in T_e anisotropy. In the southern Cordillera and across the Interior Plains all indicators align in the direction of plate motion and subduction of Juan de Fuca beneath North America, suggesting a stress control on the deformation of western Canada. (For interpretation of the references to colour in this figure legend, the reader is referred to the web version of this article.).

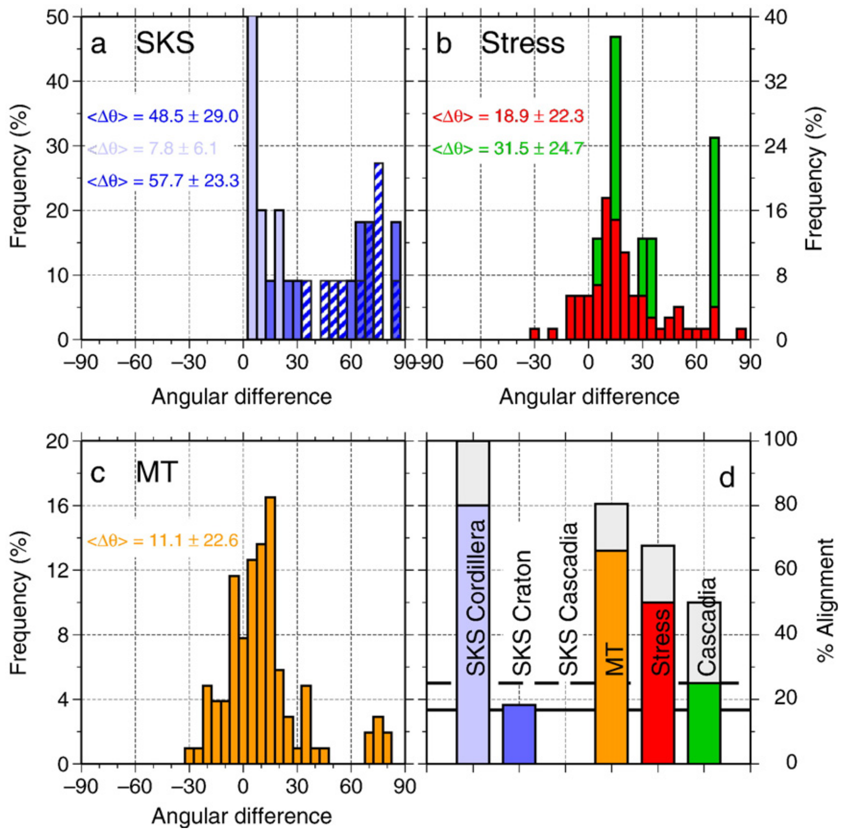

Fig. 9. Statistics of anisotropy to test whether the observed alignment between T_e weak directions and other anisotropy indicators is significant. In (a), (b), and (c) the histograms show the angular difference between the T_e weak axes and seismic fast axes, maximum horizontal compressive stress directions, and geoelectric strikes respectively. The seismic anisotropy in (a) is further divided into three regions corresponding to the Cordillera (light blue), the Craton (dark blue), and the Cascadia backarc (hatched dark blue). Shown in (d) are the percentage of alignment to within 15° (colored bins), and to within 22.5° (light gray). Continuous and dashed black lines indicate the levels at which randomly distributed alignment should fall within 15° and 22.5°. High percentage of alignment suggests a causal link between the observables.

show a quasibimodal distribution centered on ~10° and ~75° (Fig. 9a). When binned into three distinct regional clusters (Cascadia backarc, Cordilleran Front, and Craton), the alignment between T_e weak axes and the seismic fast axes in the Cordilleran portion emerges (Fig. 9a,d, light blue). The Cascadia and Craton regions show angle differences larger than 45° with a marked proportion of data towards orthogonality. However more seismic data are required to assess the general trends observed.

4. Discussion

4.1. T_e, T_c, and heat flow

The relationship between T_e and T_c requires some discussion because it provides insight into the factors that influence T_e most strongly (Burov and Diament, 1995; Lowry and Smith, 1995). That $T_e < T_c$ in the Cordillera suggests that the average elastic properties of this region are governed, in part, by the composition and constitution of crustal rocks. In contrast, the elastic properties of the Craton, where $T_e > T_c$, must involve a component of the lithospheric mantle, although the nature and extent of the mechanical coupling of the crust to the underlying lithosphere is unknown. In principle the vertical structure of the lithosphere and its influence on plate rigidity is determined, in part, locally and regionally by geology and may be complex. However, the eastward increase in T_e is significantly greater than that which is expected if plate rigidity is related to changes in T_c alone (i.e. D is not proportional to T_c^3). Indeed, the roughly factor of 2 variation in T_e is better explained by the similar variations in heat flux that will scale approximately as $1/T_e$ if T_e is proportional to the lithospheric thickness (Maggi et al., 2000). This result suggests that although a geologically complex region,

T_e is predominantly governed by temperature in western Canada, as speculated in previous studies (Hyndman and Lewis, 1999; Flück et al., 2003).

4.2. Anisotropy and stress: a primer

Seismic anisotropy refers to variations of seismic wavespeeds along different directions of propagation or polarization (Silver, 1996; Savage, 1999). The most popular method for investigating seismic anisotropy is the splitting (or birefringence) of shear-waves travelling through the mantle. In an anisotropic mantle with a horizontal axis of symmetry, the two perpendicular shear-wave polarizations will split into a fast and a slow component. The time difference between the two phases provides an estimate of the magnitude of the anisotropy, whereas the fast polarization azimuth measures the direction of the symmetry axis. Time delays and azimuths give an indication of elastic anisotropy within the lithosphere, and can thus image deformation of the rocks in the Earth's mantle.

Under the continents, the seismic anisotropy is attributed either to frozen fabric in the lithospheric mantle (Silver, 1996), or to present-day sublithospheric mantle convection (Vinnik et al., 1992). In western Canada, almost all the seismic anisotropy data are measured by the splitting of SKS phases and are interpreted to result from shear-induced lattice-preferred orientation (LPO) of olivine in the upper mantle due to viscous flow (Bank et al., 2000; Shragge et al., 2002; Currie et al., 2004). Despite the excellent lateral resolution afforded by this method, these measurements are hampered by a poor depth resolution and/or the presence of complex anisotropic layering (Park and Levin, 2002), hindering a robust estimation of the source of the anisotropy.

Electrical anisotropy is seen by the azimuthal dependence of the phase difference between the two orthogonal horizontal components (transverse electric — TE — and transverse magnetic — TM) of the time-dependent electro-magnetic (EM) fields of magnetotelluric (MT) measurements (Boerner et al., 1999; Eaton et al., 2004; Jones, 2006). The magnitude of the electrical anisotropy is generally of a few orders of magnitude, rather than a few percents as in shear-wave anisotropy, and hence rules out the possibility of an intrinsic dry crystal or grain electrical anisotropy. Electrical anisotropy may be generated by macroscopic, graphitized (resistive) shear zones within the lithosphere that mark past tectonic events (Mareschal et al., 1995), by grain-scale anisotropy of strain-induced LPO of wet olivine crystals oriented by present-day plate motion or mantle flow (Simpson, 2001), or by enhanced fluid flow in the crust and upper mantle due for example to water being incorporated into the subduction zone (Ledo and Jones, 2001; Soyer and Unsworth, 2006) or originating from a meteoric source.

MT strike directions at a particular period represent an integrative effect of the electrical structure at a broad depth range related to the diffusion of the EM fields into a conductor. However the penetration depth of the TE field can differ from that of the TM field by tens of kilometers due to strong structural heterogeneity (Jones, 2006). Electrical anisotropy data shown in Fig. 8 show the strike directions at a period of 320 s, which is broadly representative of mid-crustal depths (Boerner et al., 1999). A reliable indicator of the electrical anisotropy magnitude is the phase separation between the impedance estimates for the two transverse modes that is consistent on a regional scale. In the Interior Plains the phase difference is maximum south of 57°, and diminishes to the north and southeast (Boerner et al., 1999). Electrical anisotropy in this region requires a hydrothermal alteration event most likely related to the tectonic assembly of Laurentia circa 1850 Ma (Boerner et al., 1999). Note that the high correlation between present-day stress and MT anisotropy rather suggests a causal link and we provide an alternative explanation for the MT anisotropy in the next section.

Seismic and electrical anisotropies mostly sample upper mantle/mid-crustal materials, but although they do not measure the same physical properties, they may be measuring the response of the same causative effect. The anisotropy in T_e provides an integrated measure of the rheology of the lithosphere at crustal and upper mantle depths and thus it fills the gap between these anisotropy measurements and surface geology features (Lowry and Smith, 1995; Simons and van der Hilst, 2003).

A number of mechanisms can induce mechanical anisotropy of the lithosphere. The azimuthal dependence of the coherence between gravity anomalies and topography indicates that flexural compensation is facilitated in the direction perpendicular to the direction that has accumulated the most deformation per unit of topographic loading, which is accommodated by folding, faulting, or buckling of the crust (i.e. the weak axis is perpendicular to strike) (Simons and van der Hilst, 2003). If the preserved gravity structure reflects the current state of stress of the lithosphere due for example to plate convergence, then the weak direction aligns in the direction of maximum compressive stress (Lowry and Smith, 1995), and that of shear strain-induced seismic anisotropy if flow is parallel to convergence. High amplitude T_e anisotropy thus reflects the preserved strain field that is likely to be related to crustal stresses and associated brittle processes (e.g. faulting, seismicity) at active convergent margins.

4.3. Conceptual model of deformation

The diverse geophysical correlations of Figs. 7 and 8, and the discussion in Section 4.2, suggest a simple conceptual model for the current state of stress and the associated brittle deformation in western Canada (Fig. 10). The alignment of the seismic anisotropy data with crustal stress indicators suggests that elastic stresses, expressed as both flexurally-supported topography, and brittle failure, indicated by earthquakes, arise in response to driving plate boundary forces and retarding mantle tractions related to Cascadia subduction and associated mantle flow. The sharp and nearly factor of 10 increase in the thickness of the elastic lithosphere from the Cordillera to the Craton is interpreted to cause bending related to a compressional component of the stress field to be concentrated a couple of hundred kilometers west of the T_e gradient. The location of this stress concentration is consistent with expectations from simple calculations of the flexural characteristics of beams and plates of variable rigidity. Elastic bending stresses scale as $(E/(1-\nu^2))$ (T_e/R), where ν and R are Poisson's ratio and the radius of curvature of the deformation, and will exceed the ~30 MPa yield strength of the crust for even very small vertical deflections of the cordilleran lithosphere (i.e. for $R<O(10^4)$ km, say).

That seismicity and mechanical weakening occurs where bending stresses are maximized is thus not surprising. If the bending is simple (approximately cylindrical, Fig. 10) failure is expected to occur in tension (leading to normal faults) and compression (leading to reverse faults) in the upper and lower halves of the elastic lithosphere, respectively. Results from geologic mapping (Carr et al., 1988) and regional GPS studies are consistent with this picture and, moreover, indicate that significant upper crustal extension and normal faulting has occurred in this region over an extended period of time (Carr et al., 1988). It is worth noting that our conceptual elastic model predicts the location of failure, regardless of the amount of finite-amplitude deformation produced thereafter, which involves no elasticity.

The enhanced west–east electrical conductivity is sufficiently large to require a fluid phase (Boerner et al., 1999; Ledo and Jones, 2001; Soyer and Unsworth, 2006), where the fluids may come either from the mantle or meteoric sources. If this electrical anisotropy is explained by a conductivity that is enhanced by charge being carried by the flow of crustal fluids it is reasonable to speculate that mechanical failure of the rocks in this region leads also to fracture permeability, with enhanced flow along pre-existing grain boundaries, and that this mechanism dominates over macroscopic fluid flow along faults, which would create a NW–SE trending MT anisotropy.

Interestingly, the maximum compressive direction of crustal stress indicators in the Cascadia forearc, inferred from the splitting of direct shear-waves generated by local earthquakes (Currie et al., 2001) and in-situ measurements, are oriented in a NW–SE direction (Fig. 7b). These observations are in agreement with the forearc sliver model of Wang (1996) who predicts large arc-parallel compressive stresses due to oblique subduction. The anisotropy in T_e in this region is in agreement with the predictions and observations of crustal stresses in the Cascadia forearc.

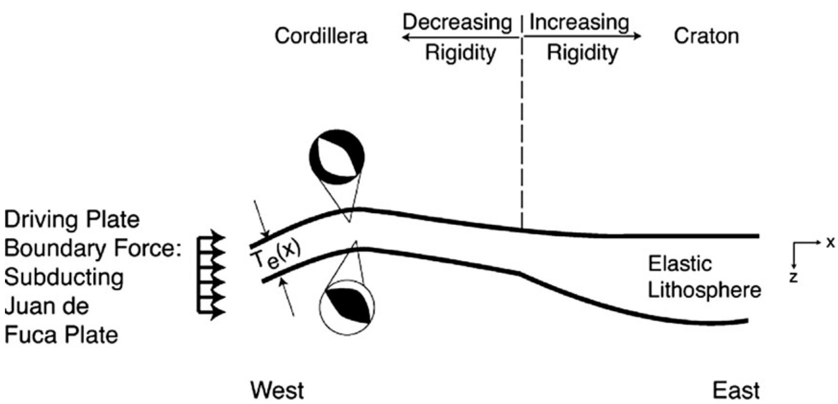

Fig. 10. Cartoon showing a geodynamic interpretation of the elastic thickness results. The driving forces for lithospheric deformation at the convergent margin of western Canada are due to the subduction of the Juan de Fuca plate beneath North America. The elastic plate flexes in response to the loads applied at the plate boundary, and the stresses concentrate where rigidity is lowest, west of the maximum gradient of T_e. Brittle failure and seismicity occur in the upper and lower halves of the plate as a result of displacement along normal and reverse faults, respectively. Note that the amplitude of the flexure is significantly exaggerated (to finite-amplitude) to highlight the underlying mechanics of the flexure and failure processes.

The northern Cordillera represents a remarkably tectonically and seismically active region where the collision of the Yakutat Block drives the deformation at least 1000 km farther inland (Hyndman et al., 2005). Our limited coverage of this region hampers a more quantitative comparison of the mechanical controls on the deformation, although the very steep gradient in T_e north of 60° suggests that the same mechanisms operate in this region (see Fig. 7). More T_e data north of 60° latitude along with constraints from other geophysical observables are needed to verify the validity of our mechanical model in the northern Cordillera.

The conceptual model explains the stress-induced deformation where the lithosphere is weakest and where deformation is most likely controlled by the rheology of the crust, but fails to explain all the features observed on the anisotropy correlation map (Fig. 8), notably in the Craton. In this region T_e is larger than T_c but much lower than the ~300 km thick lithosphere, suggesting that at least part of the lithospheric mantle contributes to the rigidity. The fact that seismic fast axes align in the direction of absolute plate motion indicates that the anisotropy is consistent with shear-induced LPO of olivine in the upper mantle due to viscous flow (Bank et al., 2000). Because the very rigid Craton largely escapes deformation and is unaffected by present-day stress levels within the lithosphere, the T_e anisotropy therein most likely reflects the fossil strain field from past tectonic events and may not correlate with the deformation associated with the present-day absolute plate motion at the base of the lithosphere (Simons and van der Hilst, 2003). On the other hand, if the seismic anisotropy were due to frozen fabric within the lithosphere, the seismic fast axes should anti-correlate with the T_e weak directions (Simons and van der Hilst, 2003). The absence of constraints from other geophysical observables renders this hypothesis difficult to assert in a testable way.

5. Conclusion

The estimation of the spatial variations of the elastic thickness is a complex spatio-spectral problem because the elastic response of the plate to loading is dominated by features with wavelengths much larger than T_e. To address this issue, we use the multitaper and wavelet transform methods to obtain detailed maps of T_e and its anisotropy in western Canada. Our results are compared to relevant data sets and suggest that under the current tectonic stress regime the locations of brittle fracturing of crustal rocks, indicated by seismicity, mechanical anisotropy, and enhanced electrical conductivity (i.e. fracture permeability), are governed by the detailed spatial variations in plate rigidity. Whether or not this simple conceptual model is validated by more thorough geodynamic modelling of the deformation of western Canada, our work indicates that an accurate determination of the spatial variations in T_e is fundamental to understanding the modern processes governing lithospheric deformation at active continental margins in general.

Acknowledgments

This paper was much improved by thorough and constructive reviews by three anonymous reviewers. This work is supported by the Natural Science and Engineering Research Council of Canada and by the Canadian Institute for Advanced Research.

References

Audet, P., Mareschal, J.-C., 2004. Anisotropy of the flexural response of the lithosphere in the Canadian Shield. Geophys. Res. Lett. 31, L20601. doi:10.1029/2004GL021080.

Audet, P., Mareschal, J.-C., 2007. Wavelet analysis of the coherence between Bouguer gravity and topography: application to the elastic thickness anisotropy in the Canadian Shield. Geophys. J. Int. 168, 287–298.

Bank, C.-G., Bostock, M.G., Ellis, R., Cassidy, J., 2000. A reconnaissance teleseismic study of the upper mantle and transition zone beneath the Archean Slave craton in NW Canada. Tectonophysics 319 (3), 151–166.

Becker, T.W., Facenna, C., O'Connell, R.J., Giardini, D., 1999. The development of subduction in the upper mantle: insights from experimental and laboratory experiments. J. Geophys. Res. 104, 15207.

Billen, M.I., Gurnis, M., Simons, M., 2003. Multiscale dynamic models of the Tonga-Kermadec subduction zone. Geophys. J. Int. 153, 359–388.

Boerner, D.E., Kurtz, R.D., Craven, J.A., Ross, G.M., Jones, F.W., 1999. A synthesis of electromagnetic studies in the Lithoprobe Alberta Basement Transect: constraints on Paleoproterozoic indentation tectonics. Can. J. Earth Sci. 37, 1509–1534.

Burov, E.B., Diament, M., 1995. The effective elastic thickness (T_e) of continental lithosphere: what does it really mean? J. Geophys. Res. 100 (B3), 3905–3927.

Carr, S.D., Parrish, R., Parkinson, D.L., 1988. Eocene extensional tectonics and geochronology of the southern Omineca Belt, British Columbia and Washington. Tectonics 7, 181–212.

Currie, C.A., Hyndman, R.D., 2006. The thermal structure of subduction zone backarcs. J. Geophys. Res. 111, B08404. doi:10.1029/2005JB004024.

Currie, C.A., Cassidy, J.F., Hyndman, R.D., 2001. A regional study of shear wave splitting above the Cascadia subduction zone: margin-parallel crustal stress. Geophys. Res. Lett. 28, 659–662.

Currie, C.A., Cassidy, J.F., Hyndman, R.D., Bostock, M.G., 2004. Shear wave anisotropy beneath the Cascadia subduction zone and western North American craton. Geophys. J. Int. 157, 341–353.

Eaton, D.W., Jones, A.G., 2006. Tectonic fabric of the subcontinental lithosphere: evidence from seismic, magnetotelluric and mechanical anisotropy. Phys. Earth Planet. Inter. 158, 85–91.

Eaton, D., Jones, A., Ferguson, I., 2004. Lithospheric anisotropy structure inferred from collocated teleseismic and magnetotelluric observations: Great Slave Lake shear zone, northern Canada. Geophys. Res. Lett. 31, L19614. doi:10.1029/2004GL020939.

Flück, P., Hyndman, R.D., Lowe, C., 2003. Effective elastic thickness T_e of the lithosphere in western Canada. J. Geophys. Res. 108 (B9), 2430. doi:10.1029/2002JB002201.

Forsyth, D.W., 1985. Subsurface loading and estimates of the flexural rigidity of continental lithosphere. J. Geophys. Res. 90 (B14), 12623–12632.

Frederiksen, A.W., Bostock, M.G., Cassidy, J.F., 2001. S-wave velocity structure of the Canadian upper mantle. Phys. Earth Planet. Inter. 124 (3–4), 175–191.

Gaspar-Escribano, J.M., van Wees, J.D., ter Voorde, M., Cloetingh, S., Roca, E., Cabrera, L., Munoz, J.A., Ziegler, P.A., Garcia-Castellanos, D., 2001. Three-dimensional flexural modelling of the Ebro Basin (NE Iberia). Geophys. J. Int. 145, 349–367.

Hyndman, R.D., Lewis, T.J., 1999. Geophysical consequences of the Cordillera-Craton thermal transition in southwestern Canada. Tectonophysics 306, 397–422.

Hyndman, R.D., Flueck, P., Mazzotti, S., Lewis, T.J., Ristau, J., Leonard, L., 2005. Current tectonics of the northern Canadian Cordillera. Can. J. Earth Sci. 42, 1117–1136.

Jones, A.G., 2006. Electromagnetic interrogation of the anisotropic Earth: looking into the Earth with polarized spectacles. Phys. Earth Planet. Inter. 158, 281–291.

Kirby, J.F., Swain, C.J., 2004. Global and local isostatic coherence from the wavelet transform. Geophys. Res. Lett. 31 (L24608). doi:10.1029/2004GL021569.

Kirby, J.F., Swain, C.J., 2006. Mapping the mechanical anisotropy of the lithosphere using a 2-D wavelet coherence, and its application to Australia. Phys. Earth Planet. Inter. 158, 122–138.

Kohlstedt, D.L., Evans, J.B., Mackwell, S.J., 1995. Strength of the lithosphere: constraints imposed by laboratory experiments. J. Geophys. Res. 100, 17587–17602.

Ledo, J., Jones, A.G., 2001. Regional electrical resistivity structure of the southern Canadian Cordillera and its physical interpretation. J. Geophys. Res. 106, 30755–30769.

Lowry, A.R., Smith, R.B., 1995. Strength and rheology of the western U. S. Cordillera. J. Geophys. Res. 100 (B9), 17947–17963.

Maggi, A., Jackson, J.A., McKenzie, D., Priestley, K., 2000. Earthquake focal depths, effective elastic thickness, and the strength of the continental lithosphere. Geology 28 (6), 495–498.

Mareschal, M., Kellett, R.L., Kurtz, R.D., Ludden, J.N., Ji, S., Bailey, R.C., 1995. Archaean cratonic roots, mantle shear zones and deep electrical anisotropy. Nature 375, 134–137.

Park, J., Levin, V., 2002. Seismic anisotropy: tracing plate dynamics in the mantle. Science 296, 485–489.

Peacock, S.M., 1990. Fluid processes in subduction zones. Science 248, 329–337.

Pérez-Gussinyé, M., Lowry, A., Watts, A.B., Velicogna, I., 2004. On the recovery of effective elastic thickness using spectral methods: examples from synthetic data and from the Fennoscandian Shield. J. Geophys. Res. 109, B10409. doi:10.1029/2003JB002788.

Pérez-Gussinyé, M., Lowry, A.R., Watts, A.B., 2007. Effective elastic thickness of South America and its implications for intracontinental deformation. Geochem. Geophys. Geosys. 5, Q05009. doi:10.1029/2006GC001511.

Perry, H.K.C., Eaton, D.W.S., Forte, A.M., 2002. LITH5.0: a revised crustal model for Canada based on Lithoprobe results. Geophys. J. Int. 150, 285–294.

Price, R.A., 1986. The southeastern Canadian Cordillera: thrust faulting, tectonic wedging, and delamination of the lithosphere. J. Struct. Geol. 8, 239–254.

Rajesh, R.S., Stephen, J., Mishra, D.C., 2003. Isostatic response and anisotropy of the Eastsern Himalayan–Tibetan Plateau: a reappraisal using multitaper spectral analysis. Geophys. Res. Lett. 30 (2), 1060. doi:10.1029/2002GL016104.

Savage, M.K., 1999. Seismic anisotropy and mantle deformation: what have we learned from shear wave splitting? Rev. Geophys. 37 (1), 65–106.

Shragge, J., Bostock, M.G., Bank, C.G., Ellis, R.M., 2002. Integrated teleseismic studies of the southern Alberta upper mantle. Can. J. Earth Sci. 39, 399–411.

Silver, P.G., 1996. Seismic anisotropy beneath the continents: probing the depths of geology. Annu. Rev. Earth Planet. Sci. 24, 385–432.

Simons, F.J., van der Hilst, R.D., 2003. Seismic and mechanical anisotropy and the past and present deformation of the Australian lithosphere. Earth Planet. Sci. Lett. 211 (3–4), 271–286. doi:10.1016/S0012-821X(03)00198-5.

Simons, F.J., Zuber, M.T., Korenaga, J., 2000. Isostatic response of the Australian lithosphere: estimation of effective elastic thickness and anisotropy using multitaper spectral analysis. J. Geophys. Res. 105 (B8), 19163–19184.

Simpson, F., 2001. Resistance to mantle flow inferred from the electromagnetic strike of the Australian upper mantle. Nature 412, 632–635.

Soyer, W., Unsworth, M., 2006. Deep electrical structure of the northern Cascadia (British Columbia, Canada) subduction zone: implications for the distribution of fluids. Geology 34, 53–56. doi:10.1130/G21951.1.

Stark, C.P., Stewart, J., Ebinger, C.J., 2003. Wavelet transform mapping of effective elastic thickness and plate loading: validation using synthetic data and application to the study of southern African tectonics. J. Geophys. Res. 108, 2258. doi:10.1029/2001JB000609.

Stegman, D.R., Freeman, J., Schellart, W.P., Moresi, L., May, D., 2006. Influence of trench width on subduction hinge retreat rates in 3-D models of slab rollback. Geochem. Geophys. Geosys. 7, Q03012.

Stern, R.J., 2002. Subduction zones. Rev. Geophys. 40. doi:10.1029/2001RG000108.

Swain, C.J., Kirby, J.F., 2003. The coherence method using a thin anisotropic plate model. Geophys. Res. Lett. 30 (19), 2014. doi:10.1029/2003GL018350.

Swain, C.J., Kirby, J.F., 2006. An effective elastic thickness map of Australia from wavelet transforms of gravity and topography using Forsyth's method. Geophys. Res. Lett. 33, L02314. doi:10.1029/2005GL025090.

Tassara, A., Swain, C., Hackney, R., Kirby, J., 2007. Elastic thickness structure of South America estimated using wavelets and satellite-derived gravity data. Earth Planet. Sci. Lett. 253, 17–36.

Thomson, D.J., 1982. Spectrum estimation and harmonic analysis. Proc. IEEE 70 (9), 1055–1096.

Vinnik, L.P., Makeyeva, L.I., Milev, A., Usenko, A.Y., 1992. Global patterns of azimuthal anisotropy and deformations in the continental mantle. Geophys. J. Int. 111, 433–447.

Wang, K., 1996. Simplified analysis of horizontal stresses in a buttressed forearc sliver at an oblique subduction zone. Geophys. Res. Lett. 23 (16), 2021–2024.

Watts, A.B., 2001. Isostasy and flexure of the lithosphere. Cambridge Univ. Press, Cambridge, UK.

Watts, A.B., Burov, E.B., 2003. Lithospheric strength and its relationship to the elastic and seismogenic layer thickness. Earth Planet. Sci. Lett. 213, 113–131.